



## Corrosion behaviour of Fe-C alloys in a Sulfuric Medium

M. Ferhat<sup>\*1</sup>, A. Benchettara<sup>1</sup>, S.E Amara<sup>1</sup>, D. Najjar<sup>2</sup>

<sup>1</sup>Laboratoire d'Electrochimie-Corrosion, Métallurgie et Chimie Minérale,  
Faculté de Chimie, USTHB, BP 32 El-Alia, Bab Ezzouar, Alger 16111, Algeria

<sup>2</sup>Laboratoire de Mécanique de Lille CNRS UMR 8107 Arts et Métiers  
ParisTech 8 Boulevard Louis XIV 59046 Lille Cedex, France

Received 25 Dec 2013, Revised 25 Apr 2014, Accepted 25 Apr 2014

\*Corresponding Author. E-mail: [m.ferhat@mail.lagh-univ.dz](mailto:m.ferhat@mail.lagh-univ.dz) (Tél. +213662111702),

### Abstract

Four different multiphase Fe-xC alloys are prepared with different ferrite and cementite amounts. X-ray diffraction analysis is used to identify the present phases in the samples. The corrosion process was evaluated by DC measurements and electrochemical impedance spectroscopy (EIS). Behaviour of Fe-xC alloys in sulfuric acid solution is greatly affected by increasing carbon concentration. Carbon increases the corrosion rate, and influences the adherence of passive film. The synergic effect of cementite is highlighted; corrosion rate is dependent on the distribution of cementite in the microstructure. The rate of the corrosion reactions increased markedly, by decreasing the average pearlite lamellae spacing in a given alloy.

*Keywords:* corrosion- microstructure- cementite - sulfuric acid-EIS

### 1. Introduction:

Alloying affects the corrosion resistance in many different ways. Changes in the nobility of the metal, the dissolution kinetics, the performance of a passive film, the phase structure of the material, the ability to catalyze the cathodic half-reaction, and other corrosion-influencing parameters. Some of these changes help to decrease or to increase the susceptibility, corrosion rate of metal in an environment, and extent of corrosion damage. The study of both, active dissolution and passive state, require the use of acid environment.

Sulfuric acid, in concentrated form, is the most produced reagent worldwide; corrosion by concentrated sulfuric acid has received little attention from researchers dedicated to the study of corrosion. In Algeria, the concern for corrosion by sulfuric acid has increased in the oil and gas industry because of the recent policy concerning the transformation (Kyoto protocol ratified in 2005), not only of carbon dioxide, but also of other greenhouse gases, like H<sub>2</sub>S and. Most of the sulfur derived from the burning of fossil fuels is emitted in gaseous form as SO<sub>2</sub>. Both the chemical composition and the physical state of the pollutants change during their transport in the atmosphere. The sulfur dioxide is oxidized on moist particles or in droplets of water to sulfuric acid. The latter, being very aggressive, attacks the metallic materials used for the construction of storage tanks and pipes. Depending on the sulfuric acid concentration range, many types of metallic materials are used to construct tanks and pipes. The most widely used alloys for handling sulfuric acid are carbon steel and austenitic stainless steels.

In steels, carbon is the most important alloying element, which has a different solubility in the various phase of iron. Changing the carbon content is a simple method for the production of different kinds of microstructures. In this work four alloys with a difference in carbon content are selected.

This article provides an overview of the ways in which the metallurgical variables, namely composition and structure, influence the corrosion properties of Fe-xC alloys in sulfuric acid medium. The adherence of the corrosion film, and hence its protectiveness, have often been related to the presence of cementite and its morphology (lamellar, globular, etc.). The size and distribution of this cementite can affect the adherence of passive film [1]. It has reported that in the presence of ferritic phase, the corrosion resistance increases with decreasing carbon concentration [2]. Abdul Azim [3] found that the influence of carbon content on corrosion resistance of steel in HCl solutions is most pronounced when cementite exists as a separate phase. However, there are also some investigators holding the opposite views. Nestic and Lunde [4] in their studies on corrosion of carbon steel in biphasic flow at pH 4–7 and T= 20–80°C, found that the formation of protective films is difficult; cementite may have a negative role by accelerating corrosion by galvanic action.

Generally in acids, the corrosion rate depends on the composition as well as the structure of the steel and increases with carbon content. The extent of the increase depends largely on prior heat treatment; on slowly cooling carbon steel from the austenite, cementite, in part, assumes a lamellar shape, forming pearlite. This structure again corrodes at a comparatively low rate because of the relatively massive form of cementite formed by decomposition of austenite compared with smaller-size cementite particles resulting from decomposition of martensite. Corrosion rate increases as the size of cementite particles decreases. Pearlitic structures corrode faster than spheroidized ones, and steels containing fine pearlite corrode more rapidly than those with coarse pearlite. The importance of the amount of cementite acting as cathode and its state of subdivision both supports the electrochemical mechanism of corrosion. Only few studies have been devoted to determine the effects of metallurgical variables on corrosion characteristics in acid medium [5]. In deaerated acid solutions, composition and structure influence the corrosion rates of steels, as evidenced by the wide variations observed between nearly identical samples [6]. These factors affect both anodic and cathodic activation-controlled processes in a complex way, as shown by Lot [7]. However, in the presence of dissolved oxygen, the reaction is often cathodically controlled by oxygen concentration polarization (limiting diffusion current). Thus, the corrosion rates of many systems are controlled by the mass transport of dissolved oxygen to the reacting surface. In the case of ferrous alloys (including steels and cast irons), the corrosion products (iron oxides) on the surface are more or less hydrated and have different crystallographic structures. In fact, in the acid range of pH (approximately < 4) where residual elements have an active role in the *Hydrogen Evolution Reaction* (HER), differences in manufacture affect the corrosion rate. A relatively pure iron corrodes in acids at a much lower rate than an iron or steel high in residual elements, such as, carbon, nitrogen, sulfur, and phosphorus.

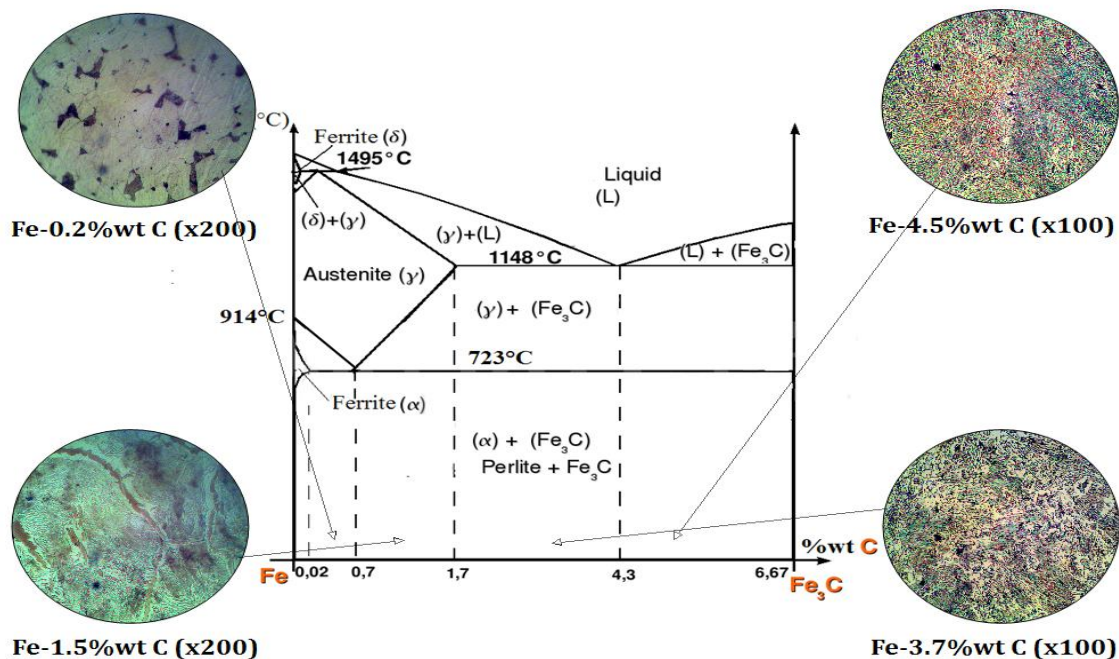


**Figure 1:** Fe-C phase diagram and microstructures

Cast iron is the term applied to a wide range of ferrous alloys, whose principal distinguishing feature is carbon content in excess of ~1.7%. The essential difference between the corrosion of cast iron and steel arises from the fact that cast iron contains in its microstructure several more or less corrosion-resistant phases that are largely absent from steel. For example, on grey cast irons, severe galvanic corrosion occur which is called graphitic corrosion, due to the presence of multiple phases [8]. Currently, no systematic study of the Fe-C alloys with the carbon, concentration higher than 1.5 wt %, is at hand. The effect of alloying Carbon on the resistance to corrosion of cast iron alloys in sulfuric media has not been clarified sufficiently. The purpose of this investigation is to determine the corrosion characteristics of full range of carbon (0.2, 1.5, 3.7, 4.5 %wt C). According to the Fe-C system phase diagram, our study focused on four regions according to their

microstructure; hypoeutectoid (0.2% wt C), hypereutectoid (1.5% wt C), and cast iron region (3.7 and 4.5% wt C) (Fig-1). This selection makes the quantity of cementite increase and the structure change from the ferritic to the ferrite–cementite one corresponding to the carbon content. The results of this research provide the criteria to utilize this carbide to improve the corrosion and wear properties, depending on the microstructural features of its microstructures.

## 2. Materials and methods

Four different multiphase alloys are used throughout this study, while pure iron is taken as a reference base material. Fe-xC alloys with different compositions (x= 0.2, 1.5, 3.7 and 4.5 C wt.%) are prepared by melting high purity elements: Fe (Aldrich 99.89%) and graphite in water-cooled copper crucible by electromagnetic high frequency induction under argon atmosphere giving master ingots. Pieces of about 30 g of Fe(C) alloys with variations in carbon content, and pure iron (Table-1), compositions are re-melted by high frequency induction and injected under argon pressure of about 0.3 MPa into water-cooled copper mould to obtain ingots. The alloy ingots are subsequently encapsulated in quartz tube under vacuum (due the high reactivity of iron with oxygen at high temperatures) and heat treated in furnace at 500°C for 1h and at 800°C for 1h and air-cooled afterward to achieve a better equilibration of the alloy phases. After the heat-treatment, the alloys are machined using an electrodischarge machine (EDM) to obtain samples in the form of 10 mm diameter disks. For both metallographic characterisation and electrochemical measurement, the specimens are respectively, hot and mounted in resin, four samples are prepared for each alloy to guarantee the reliability of the conclusions. Microstructures of the samples are studied using metallographic samples prepared by sequential polishing with silicon carbide emery paper followed by diamond polishing [9]. The preparation of cast iron alloys (i.e. %wt C =3.7 and 4.5) is difficult, retention of graphite in cast iron is a common polishing problem that has received considerable attention [10,11]; so after cleaning, the specimens are rough polished on rotating wheel covered with napless cloth and charged with micro-graded diamond abrasive. Polished samples are etched using 4% Nital (96 mL ethanol, 4 mL nitric acid) for 30s. An average grain size of each alloy was determined according to ASTM standard E112-96. X-ray diffraction analysis is used to identify the present phases in the samples, and it's performed on a Philips X-Pert diffractometer with CoK<sub>α</sub> radiation.

**Table 1:** Composition of the alloys

Alloy	Fe		C		Microstructure
	wt%	at%	wt%	at%	
Pure Iron	100	100	-	-	
Fe-0.2%wt C	99.8	99.08	0.2	0.92	ferrite+ pearlite
Fe-1.5%wt C	98.5	93.38	1.5	6.62	unresolved pearlite
Fe-3.7%wt C	96.3	84.83	3.7	15.17	decomposed pearlite
Fe-4.5%wt C	95.5	82.01	4.5	17.99	Primary cementite + graphite flakes

The potentiodynamic polarization tests are carried out using an EG & G Potentiostat/Galvanostat Model 273A corrosion measurement system, driven by 352 SoftCorr-3 software, electrochemical impedance spectroscopy (EIS) measured using PGZ 301 Potentiostat/Galvanostat and a Solartron 1255 frequency response analyzer with Volta master 4 software. EIS is recorded at open circuit potentials, in the frequency ranging from 100 kHz to 10 mHz, with a sinusoidal signal perturbation of 10 mV. The software ZView 2.3 (Scribner Associates) is used for analyzing the EIS results. In this case, the impedance plot forms a semicircle, the diameter which gives the charge-transfer resistance  $R_{ct}$ . This can be used in a Stern-Geary type equation to determine the corrosion current density,  $I_{cor}$ , and thus the corrosion rate:

$$i_{cor} = (\beta_a \cdot \beta_c) / 2.3(\beta_a + \beta_c) R_{ct} \quad (1)$$

Where  $\beta_a$ ,  $\beta_c$  are respectively anodic and cathodic slope.

The alloy mechanically ground with emery paper up to 1200 grit, degreased in acetone, rinsed with bidistilled water, dried and transferred quickly in a Tacussel glass cell filled with 100 mL of 1N sulfuric acid solution. A saturated sulfate electrode (SSE) and graphite electrode are used as reference and auxiliary electrodes, respectively. All measured potentials are reported to this reference electrode. At each potentiodynamic polarization, the samples are kept at the free corrosion potential for 30 mn and then the cyclic polarization responses are measured from -250 with respect to the corrosion potential to 1600mV/SSE and back of each sample in 1 N sulfuric acid medium conducted at a sweep rate of 0.5 mV/s.

### 3. Results and discussion

#### 3.1 Metallographic measurements

Carbon steel (Fe-0.2% wt C) is referred to hypoeutectoid, the structure consists essentially of ferrite (white) and pearlite (dark) Fig-2(a). When carbon content is above 1.5% wt, i.e. alloy Fe-1.5C, this alloy is referred to as hypereutectoid Fig-2(b). The structure is unresolved pearlite (dark) with cementite (white) at prior austenite grain boundaries. The ferrite and cementite phases show the same white when the samples are etched using 4% Nital, so the proeutectoid cementite phase can be observed in alloy Fe-1.5C using the XRD, as shown in Fig-3. In Fe-3.7% wt C alloy, the cementite is not uniformly distributed. The most of pearlite has decomposed into matrix, so the structure is a mixture of lamellar pearlite and spheroidal cementite in a matrix of ferrite Fig-2(c). Alloy Fe-4.5% wt C reveals ferritic iron with primary cementite, other constituents are carbon graphite and a ferrite matrix Fig-2(d). The pearlite distribution seems to increase with the increasing in carbon content. In addition, the pearlite structures are finer and more uniformly distributed in ferrite matrix.

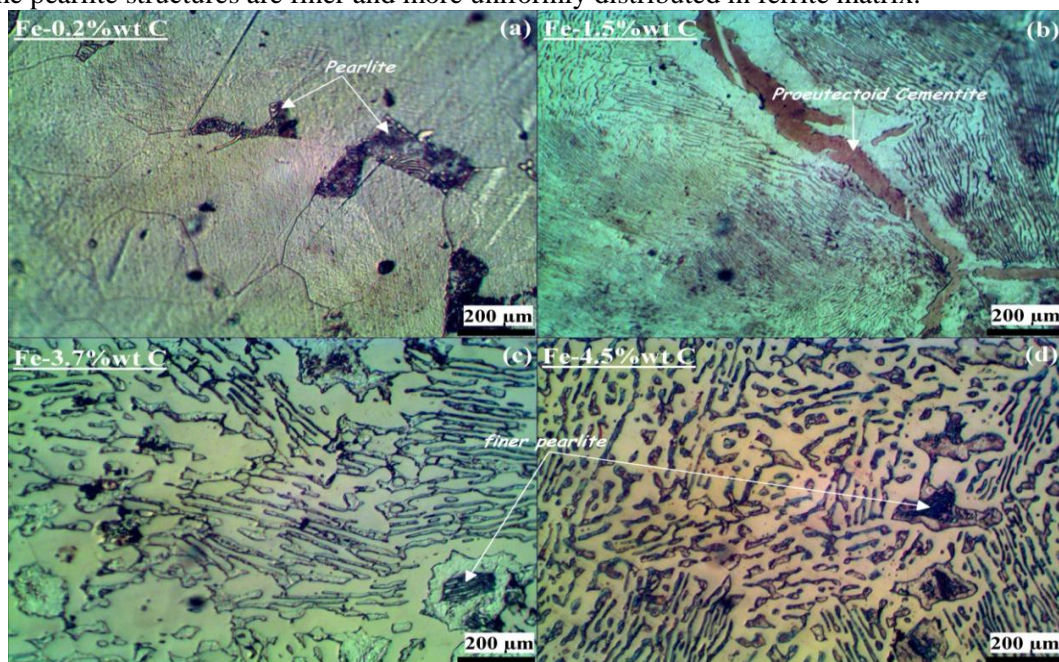


**Figure 2:** Optical micrograph of Fe-xC alloys, etched with 4% Nital

The XRD curve of the F(C) in Fig-3 mainly constituted of the two peaks. The peaks numbered 1 and 2 refer to the ferrite and cementite phase respectively. It can be seen that all Fe-xC alloys have a predominant primary  $\alpha$ -Fe phase, in addition to cementite phase. The iron diffraction peaks broaden and their intensities decrease with increasing in carbon content. However, a decrease in the intensity of the peaks of cementite in Fe-4.5% wt C alloy is noted. Excess carbon might exist in the substrate as free carbon, which it does not detected by XRD. This finding is in agreement with literature; cementite exceeds its solubility in solid iron and dispersed as graphite [12].

#### 3.2 Electrochemical behaviour of alloys:

##### 3.2.1 EIS measurements :

Electrochemical impedance spectroscopy is employed to investigate the film/electrolyte-interface, on the Fe-xC alloys in 1 N sulfuric acid solution. Fig-4(a) shows the Nyquist plots (imaginary part of impedance vs. real part of impedance, at different frequencies) of the five Fe-xC alloys. The impedance parameters obtained following the fitting of the EIS experimental results by using the EC displayed in Fig-4(d) are listed in Table 2. Where  $R_s$  is the electrolyte resistance,  $Q_{dl}$  is a constant phase element (CPE) representing the double-charge layer capacitance,  $R_{ct}$  is the charge transfer resistance,  $R_L$  is the inductive resistance and L is the inductance. The CPE impedance ( $Z_{CPE}$ ) is described by Eq. (3) as follows:

$$Z_{CPE} = (jQ\omega)^{-n} \quad (2)$$

Where  $Z_{CPE}$  is the impedance of CPE,  $Q$  is a proportional factor (CPE), “ $j$ ” is  $\sqrt{-1}$  and  $\omega$  is  $2\pi f$ , and  $n$  is a factor which takes values between 0 and 1.

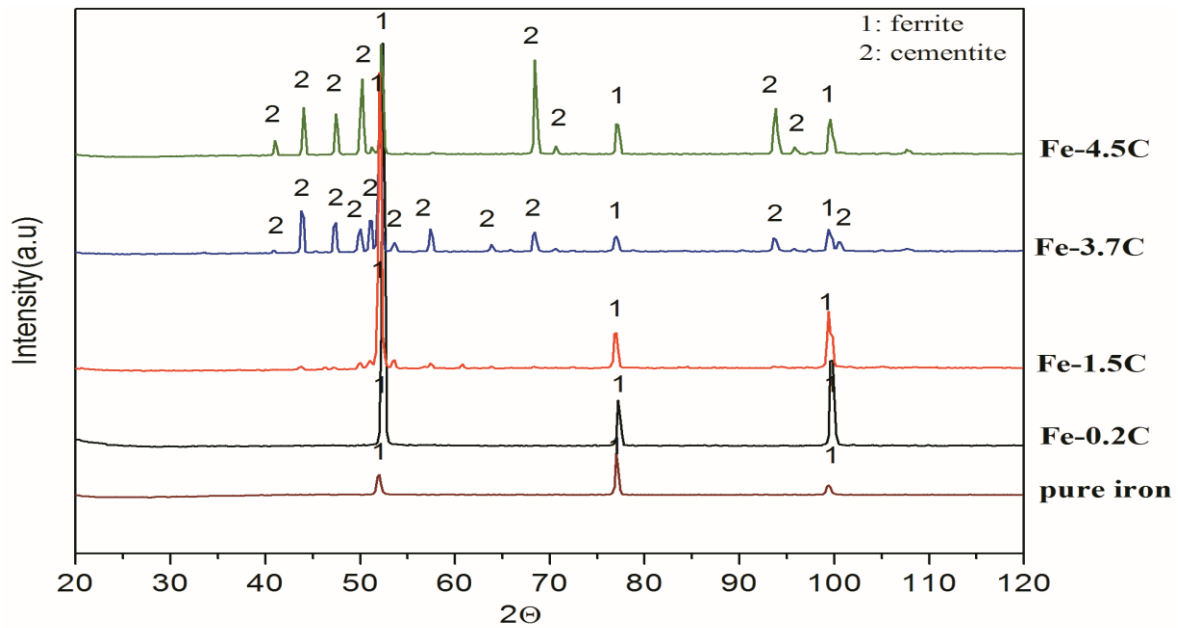


**Figure 3:** X-ray diffraction patterns of five samples of Fe-xC alloys

The values of slope are less than one in a plot of  $\log(Z_j)$  ( $\Omega.cm^2$ ) versus  $\log f$  (Hz) in all the studies samples indicating the existence of a constant phase element [13, 14]. When the imaginary part of the impedance is independent of the electrolyte resistance, the slope is constant in the frequency range. Two time constants are identified on Fig-4(a), a capacitive half circle in the high (HF)–medium (MF) frequencies range, and an inductive loop in the low frequency (LF) range. The inductive behaviour at low frequencies is detected in all obtained EIS tests except for pure iron. This inductive loop can be modelled by a parallel inductance (L) and resistance ( $R_L$ ). Some authors assigned it to the relaxation of the intermediates belonging to the adsorption phenomenon leading to a secondary passivity in the transpassive peak region, as indicated by many authors [17, 18]. According to A.Anejjar et al [19], the state is an active adsorption. The capacitive half circle characterizes the active state of the interface when steels are exposed to sulfuric acid solution 1N. The amplitude of the loop decreases when C-content increase from pure Iron to Fe-4.5 wt% C alloy except the Fe-3.7%wt C alloy, indicating that the charge transfer process assumed to be the cathodic reaction or hydrogen reduction is more favorable. This behaviour has been related, by Lopez et al [1] to the presence of cementite. Cementite serves as an electronic conductor where the reduction of hydrogen ions takes place, as suggested by Matlosz et al. [20]. Cementite forms preferential cathodic sites with lower overpotential favouring hydrogen evolution. This leads to microgalvanic cells between Cementite and ferrite phase ( $\alpha$ -Fe); resulting in selective dissolution of ferrite and in an influence on the kinetics by galvanic effect [21, 22]. The effect of cathodic regions associated to the cementite is considerable in carbon alloys with carbon content higher than 0.2% wt [23]. The behaviour at high frequencies of Fe-1.5%wt C, Fe-3.7%wt C, and Fe-4.5%wt C alloys are independent of C-content (see enlargement Fig-4(a)), an increase of cementite in iron alloys does not have a significant influence on the diameters of the capacitive loop. The corrosion rate does not depend on the quantity of cementite. However we shall note the light increase in  $R_{ct}$  value on Fe-3.7% wt C alloy. The small decrease in the corrosion rate is due to the disruption of the *HER* as will be demonstrated later from the Tafel curves. At LF the inductive loop, has been associated to the adsorption of an intermediate product, according to Farelas et al [24] the intermediate product may be  $FeOH_{ads}$ . Fig-4(b and c) shows the phase angle and Bode representation of the EIS spectra, respectively. Phase angle representation in Fig-4(b) shows at HF–MF magnitudes characteristic of charge transfer process due to dissolution process. The phase angle evolution at LF shifts from negative to positive quadrant. Such transition is attributed to the control mechanisms at the interface. The continuous formation of cementite resulted in higher number of sites favorable for adsorption reaction and less favorable for the overall charge transfer process. These parameters support the evolution of the active-adsorption surface resulted by the surface modifications for the cathodic reaction by assuming that the *HER* is the cathodic reaction [25] and controls the interfacial process. The reduction of  $H^+$  ions controls the interfacial process due to continuous dissolution of ferrite and the higher area of cementite.

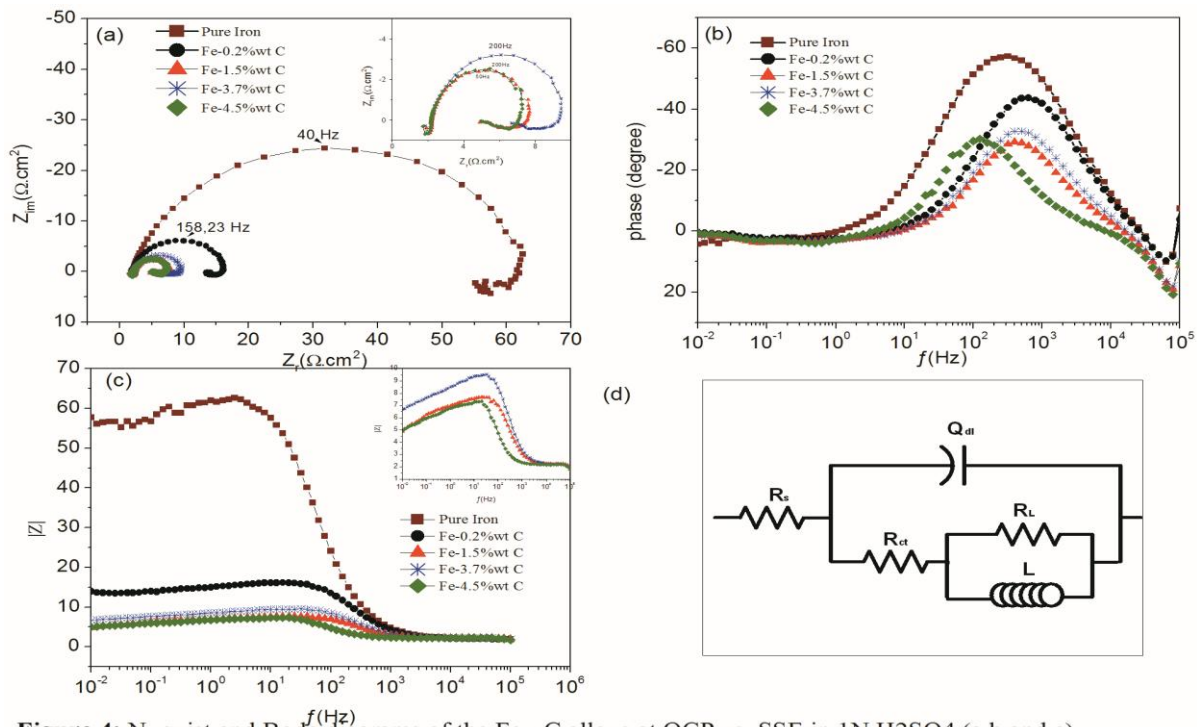


**Figure 4:** Nyquist and Bode diagrams of the Fe-xC alloys at OCP vs. SSE in 1N H<sub>2</sub>SO<sub>4</sub> (a,b and c). Equivalent circuit used to simulate the EIS diagrams obtained from Fe-xC alloys in 1N H<sub>2</sub>SO<sub>4</sub> (d).

**Table 2:** Electrochemical parameters deduced by Tafel and EIS method for Fe-xC in 0.5M H<sub>2</sub>SO<sub>4</sub>

Alloy	$E_{cor}$ mV/SSE	Polarization				EIS					
		$\beta_a$ mV/dec	$\beta_c$ mV/dec	$R_p$ $\Omega \cdot \text{cm}^2$	$i_{cor}$ mA/cm <sup>2</sup>	$R_s$ $\Omega \cdot \text{cm}^2$	$R_{ct}$ $\Omega \cdot \text{cm}^2$	$R_L$ $\Omega \cdot \text{cm}^2$	$L$ H.cm <sup>2</sup>	$Q_{dl}$ $\mu\text{F}/\text{cm}^2$	$n$
Pure iron	-885	37.4	197.8	59.06	0.25	1.985	53.68	7.42	5.76	147.32	0.85
Fe-0.2C	-801	118.2	415.2	15.2	3.38	1.961	11.85	2.33	0.41	120.14	0.90
Fe-1.5C	-692	192.9	277.6	9.63	14.91	2.261	3.32	1.75	1.27	162.31	0.96
Fe-3.7C	-666	242.3	414.9	8.15	13.13	2.222	5.07	1.92	0.52	161.32	0.93
Fe-4.5C	-640	272.1	348.9	8.91	19.75	2.174	3.37	1.58	0.68	509.93	0.96

Generally the fitting results clearly show that as  $Q_{dl}$  increases (120.14 to 509.93  $\mu\text{F} \cdot \text{cm}^{-2}$ ),  $R_{ct}$  reduces (11.85–3.37  $\Omega \cdot \text{cm}^2$ ), from 0.2% Wt C and up to the 4.5%Wt C. This  $Q_{dl}$  behaviour is due to the physical–electrical properties of the corrosion products.  $Q_{dl}$  is directly proportional to the area available for the HER. The great values of  $Q_{dl}$  obtained for the Fe-4.5 %wt C alloy, is attributed to the increased surface area available for the cathodic reaction, and the results clearly indicate the electrochemical activity of the cementite residues. The lowest  $Q_{dl}$  value is obtained for Fe-0.2 %wt C alloy, which indicates the decrease in local dielectric constant due to the low quantity of pearlite. However, a little decrease in  $Q_{dl}$  value (161.32  $\mu\text{F} \cdot \text{cm}^{-2}$ ) is identified for Fe-3.7%wt C alloy. These electrochemical differences may be related to the microstructure of this alloy; the pearlite initially formed has decomposed into matrix separately in this alloy, so less area available for the HER and little increase in the corrosion resistance. In fact, corrosion resistance does not only dependent on the quantity of cementite, but also on its distribution in the microstructure. The decrease of  $R_{ct}$  values is a consequence of the continuous dissolution of the ferrite phase, due to the increase of the cementite area which enhance the galvanic effect of cementite [26,27].  $R_L$  is directly proportional to the coverage of  $FeOH_{ads}$  at the surface. And its values correspond approximately to the resistance of the electrolyte ( $R_s$ ). The values of  $R_L$  in Fe-1.5%wt C, Fe-3.7%wt C, and Fe-4.5%wt C alloys are less than  $R_s$ ; we suppose that the outer layer is very porous.

### 3.2.2 Polarisation studies of Fe-xC alloys

Cyclic polarization curves for the Fe-C alloys studied are shown in Fig-5. The corrosion parameters of Fe(C) alloys as obtained from the polarization curves (Fig-6) are collected in Table-2. Curves show a typical current-potential ( $i-E$ ) polarization. These curves can be useful from a kinetic and thermodynamic point of view (table-

3). Several characteristic regions can be distinguished, where different processes occur in agreement with previous studies [28-30]: an active dissolution region, where the current increases exponentially with potential according to Tafel law; and an ohmic controlled region where the current increases linearly with potential, before reaching a peak value. In the present work two peaks appears; this will be discussed below. After the first peak potential,  $E_p$  (Fig-7), the anodic current decreases towards a lower value corresponding to the formation of a ferrous sulfate layer. After this peak, in two cases (i.e. pure iron and Fe-3.7%wtC alloy) the current shows significant oscillations due to a cyclic sequence of dissolution and precipitation of the ferrous salt layer.

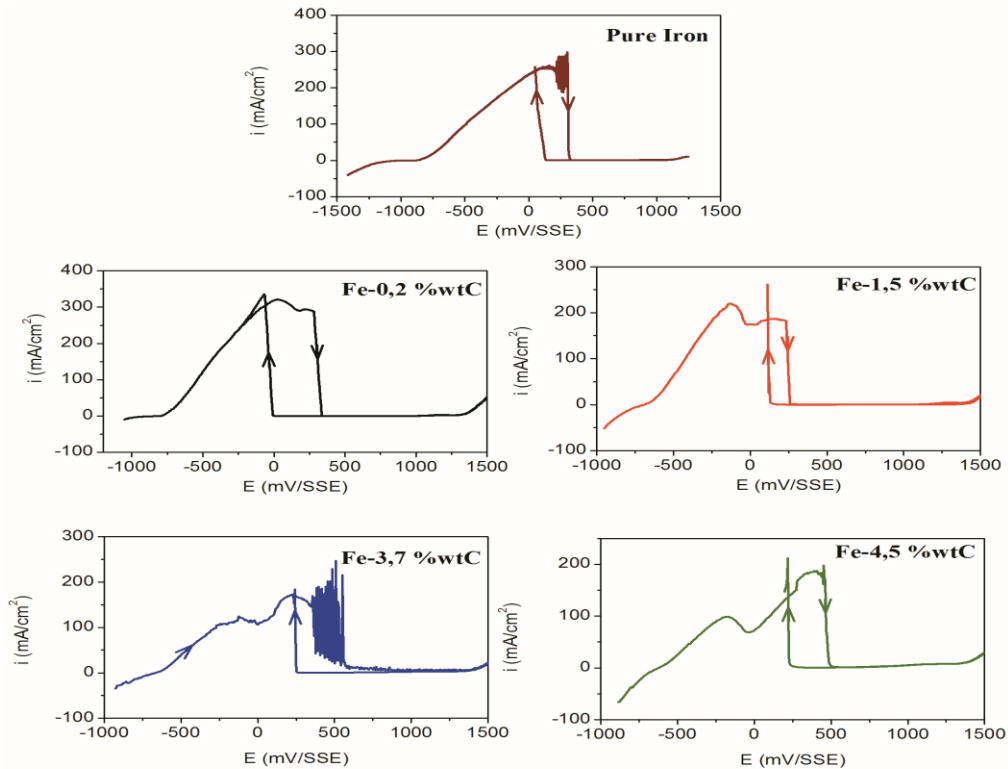


**Figure 5:** I-E cyclic polarization curves of the Fe-xC|1N H<sub>2</sub>SO<sub>4</sub> system at scan rate of 0.5 mV/s

The atypical microstructure of Fe-3.7%wtC alloy promotes the oscillations phenomenon. In this case and in agreement with Song et al [31] and Sazou and Pagitsas [28], it is assumed that a dynamic equilibrium between dissolution and formation of the ferrous sulfate salt is established at the interface between the electrode and solution. The oscillations phenomenon can be subject to a more detailed study. After this competition between dissolution and formation of a ferrous sulfate salt, a passive region is observed after a primary passivation potential  $E_{pp}$  mentioned on the Fig-7. After this potential, the passive region begins, corresponding to the formation of the iron oxide or hydroxide film and passivation of the Fe-xC electrode. Then, a transpassive region corresponds to the oxide dissolution. During the backward potential scan towards negative potential, the cyclic polarization does not show tendency to repassivation once the absence of the pitting potential. An activation of the samples electrodes takes place at a  $E_F$  (Flade potential). This hysteresis loop formed across the passive–active transition region, are potential attributed to the existence of a higher ohmic potential drop (IR) along with a higher pH value at the vicinity of the electrode at the point  $E_{pp}$  as compared with the IR-drop and pH values at the point  $E_F$ . The higher IR-drop is due to the higher current at active region (ohmic control) than at the passive state, while the higher pH is assigned to the migration of  $H^+$  ions away from the surface in order to maintain electro neutrality as  $Fe^{2+}$  ions are produced at the active region [32, 33]. The negative value of  $E_F$  -59 mV/SSE calculated for Fe-0.2 %wt C, indicates conditions more favorable to passive film formation; thereby reducing the overall free energy of the system, and hence, greater stability of passivity. Flade potential of Fe-1.5%wt C, Fe-3.7%wt C and Fe-4.5%wt C alloys, range from 117 mV to 221 mV for 4.5%wt carbon alloy. The Flade potential of steel iron alloys is less noble than cast iron. The passivation current calculated, increases sharply from 0.2% wt C ( $i_{pp} = 103 \mu A/cm^2$ ), almost double for Fe-1.5% wt C, and fifteen times higher for the carbon content for Fe-4.5% wt C. the dispersed pearlite (i.e. in Fe-0.2%wt C) reinforces the passive film more

strongly than do the accumulation of cementite (i.e. in cast iron alloys). In the case of Fe-3.7% wt C alloy, the oscillation phenomena seems to cause passive film destabilization. The two peaks appeared during the anodic dissolution of iron-carbon alloys, (Fig-7), are quantified by the currents maximum ( $i_{max1}$  and  $i_{max2}$ ) at respectively potential ( $E_p$  and  $E_{pp}$ ) in a range of minus 0.2 to plus 0.5 V/SSE, except the pure iron. As is shown in [34], the consecutive oxidation of first the ferrite phase, which results in the appearance of the first current maximum and then, the cementite phase accompanied with the formation of the second maximum. In steel alloys iron with 0.2% and 1.5% wt C we have  $i_{max1} > i_{max2}$ , contrary to cast iron (i.e. 3.7% and 4.5% wt C), where  $i_{max1} < i_{max2}$ . This behaviour is predictable, since in the case of cast-iron alloys, the oxidation of cementite is more pronounced, and therefore  $i_{max2}$  tends to increase.

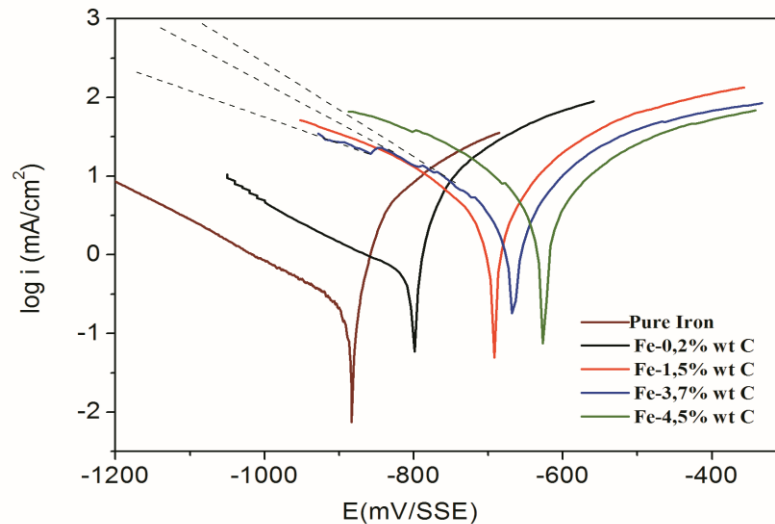


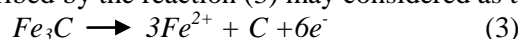
Figure 6: Potentiodynamic polarization curve obtained for Fe-C alloys in naturally aerated 0.5M H2SO4 system at a scan rate of 0.5 mV.s<sup>-1</sup>

Table 3: Different potentials calculated from cyclic curves I-E of the Fe(C) alloys

	$E_{cor}$ (mV/SSE)	$E_{Flade}$ (mV/SSE)	$E_p$ (mV/SSE)	$E_{pp}$ (mV/SSE)	$i_{pp}$ ( $\mu A/cm^2$ )
Pure iron	-885	50	150	308	153
Fe-0.2% wt C	-801	-59	21	281	103
Fe-1.5% wt C	-692	117	-132	233	228
Fe-3.7% wt C	-666	239	-123	552	4300
Fe-4.5% wt C	-640	221	-127	453	1636

The decrease in  $i_{max1}$  value from ferrite-pearlitic to pearlite-cementite structures, make us confirm that the appearance of the first current maximum in the anodic curves of the alloys is due to the anodic dissolution and passivation of only the pearlitic phase [35]. These means that ferrite in the pearlite is most inclined to the dissolution (so that the decomposition occurs at the ferrite/cementite boundaries); while the cementite phase remains active. Since the potentials of ferrite and cementite are different [36]. This indicated that pearlitic structures corrode faster than spheroidized ones; alloys containing fine pearlite corrode more rapidly than those with coarse pearlite. At  $E_{pass1}$  the ferrite phase of the alloy is passive, and at  $E_{pp}$  the process on cementite destroys the integrity of the low-soluble iron sulfate (II) layer at the ferrite/cementite boundary.

This results in opening up the adjacent ferrite areas. Possible cementite oxidation processes as represented in the E-pH diagram [37], process described by the reaction (3) may be considered as thermodynamically probable



The protective properties of the passive film in Fe-3.7C and Fe-4.5C alloys are meaningless compared to the steel alloys. The dissolution involves carbon accumulation at the surface. As is shown in [38], carbon which accumulates during the dissolution of cementite increased the defectiveness of the passive film; according to Syugaev [34] carbon promotes the stronger hydration of the passive film, which substantially increases the rate of dissolution of the passivating oxide and decreases the protective properties of the passive film which is corroborated by the data of impedance spectroscopy, where a decrease in corrosion resistance is observed (Fig.4 (a)).

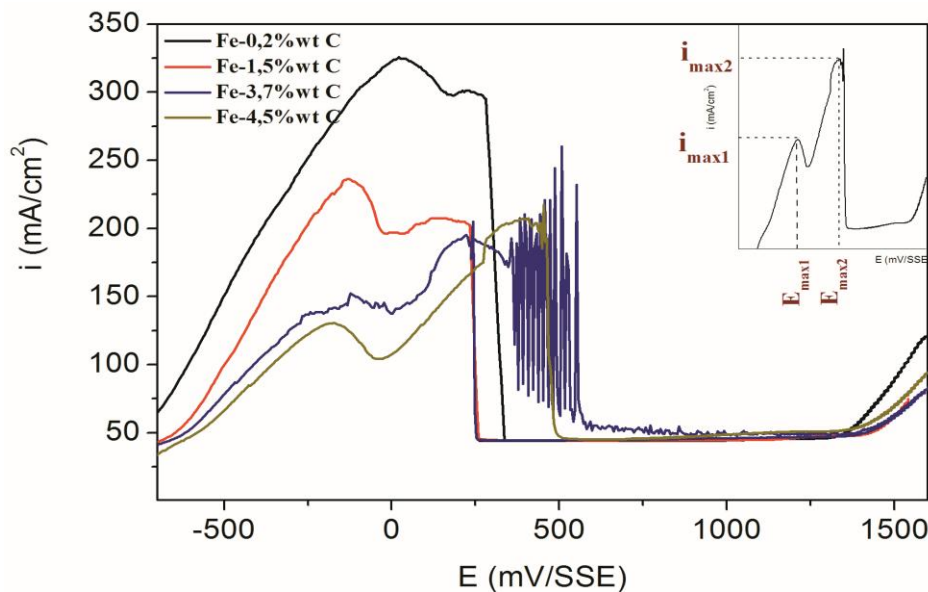


**Figure 7:** I-E anodic polarization curve of the Fe-xC|1N H<sub>2</sub>SO<sub>4</sub>. I-E curve indicate main changes in physicochemical processes occurring during polarization

Generally Tafel slope value of cathode is greater than that of the anode, which manifests the complex nature of the reduction process. The relevant electrochemical parameters obtained from the curves are listed in Table 2; The Tafel slope,  $\beta_c$ , for these materials are different to the theoretical value of 120 mV for one electron involved in the charge transfer controlled reaction, as for the alloys steel and cast-iron alloys,  $\beta_c$  shows slightly higher value than the pure iron does. The  $\beta_c$ , which is connected with the kinetics of the HER, shows similar catalytic activity of this series of alloys with different microstructures and different compositions. It is evident that the increases of carbon, both anodic and cathodic reactions of the samples are effectively affected. In steel alloys the cathodic branch of polarization curves given rise to parallel lines with increasing carbon content, which reveals that the cathodic hydrogen evolution mechanism is not changed and the hydrogen evolution is dominated in the active process. However, this is not the case in cast iron alloys; small deviations on the cathodic slopes are found, more pronounced in Fe-3.7%Wt C alloy (indicated by dashed lines on fig-6). The cathodic reaction have been greatly affected by the grain size of specimens; the cementite is not uniformly distributed so less area available for the HER. The most significant results is that cast-iron alloys have a small grain size, which have a higher number of activated sites and accelerates corrosion by forming much more microelectrochemical cells between the huge amount of grain boundaries and the matrix and by increasing the electrochemical reactivity of cementite during the corrosion process as mentioned by W. Liu et al [39].

## Conclusion

In this work, four binary alloys, containing 0.2%, 1.5% C, 3.7% C and 4.5% Wt C are produced. These materials are selected in four regions according to their microstructure. It was found that metallurgical structure has a marked effect on the corrosion rate, the importance of both the amount of cementite acting as cathode and its state of subdivision supports the electrochemical mechanism of corrosion.

Results summarized as follows:

1. Hypoeutectoid structure, the alloys with low percentage of carbon (0.2 %wt), the pearlite is completely resolved into matrix; it promotes the easier passivation and the more stable passivating film, the lowest  $I_{pp}$  ( $I_{pp} = 103 \mu\text{A}/\text{cm}^2$ ), In this case, cementite provides the best state of passivity.
2. The impedance response of electrochemical systems, allow a good evaluation of the degree of distribution of the cementite. These distributions can lead to CPE behaviour.
3. Decomposition of pearlite into matrix as the separate precipitates, microstructure close to the eutectic (3.7%wt C), promotes the oscillation phenomenon, and negatively affects the passivation proprieties (slightly high value of  $I_{pp} = 4300 \mu\text{A}/\text{cm}^2$ ).
4. Corrosion of cast irons structures does not appear to be strongly dependent on the total amount of cementite; but to the grain size of specimens. The corrosion rate always increases as the size of cementite particles decreases.

**Acknowledgement**-The authors would sincerely like to thank Dr Aboki Tiburce “Laboratoire de métallurgie structural” ENSCP Paris, France for his help in the smelting of alloys.

## References

1. López D. A., Schreiner, W.H., De Sánchez, S.R., Simison, S.N., *Applied Surface Science*. 207 (2003) 69–85.
2. Guo J., Yang, S., Shang, C., Wang, Y., He, X., *Corrosion Science*. 51 (2009) 242–251
3. Azim, Sanad, S.H., *Corrosion Science*. 12 (1972) 313-324.
4. Nestic, S., Lunde, L., *Corrosion*. 50 (1994) 717–727.
5. Fiaud, C., Safavi, M., Vedel, J., *Journal of Materials and Corrosion* (2004) 361–366
6. Kwok, C.T., Leong, K.I., Cheng, F.T., Man, H.C., *Materials Science and Engineering A*. 357 (2003) 94–103.
7. Loto, R. T., *Journal of Materials and Environmental Science*, 4 (2013) 448-459.
8. Banas, J., Mazurkiewicz, A., *Materials Science and Engineering A*. 277(2000) 183-191.
9. ASM Handbook, Volume 9 Metallography and Microstructures 9<sup>th</sup> ed, (1992) 280.
10. Radzikowska, J. M., *Materials Characterization*. 54 (2005) 287– 304.
11. CHE L., GOTOH, M., HORIMOTO, Y., HIROSE, Y., *Iron and Steel*. 14(2007) 31-38
12. Zuhailawati H., Geok, T., Basu, P., *Materials and Design*. 31 (2010) 2211–2215.
13. Chetouani A., Aouniti, A., Hammouti, B., Benchat, N., Benhadda, T., Kertit, S., *Corrosion Science*. 45 (2003) 1675–1684
14. Lai-zhou S., YANG Z.Y., *Iron and Steel* 16 (2009) 89-94.
15. Song G., Bowles, A. L., St John, D. H., *Materials Science and Engineering A*. 366 (2004) 74–86
16. Duan H.P., Li, Y. C., Yan, C.W., *Mater Sci*, 10 (2005) 2911-2917
17. Frateur I., Lartundo-Rojas L., Méthivier C., Galtayries A., Marcus P., *Electrochimica Acta*, 51 (2006) 550.
18. Ahlberg, E., Friel, M., *Electrochim Acta*. 34 (1989) 1523–1528.
19. Anejjar A., Zarrouk, A., Salghi, R., Zarrok, H., Ben Hmamou, D., Hammouti, B., Al-Deyab, S. S., *Journal of Materials and Environmental Science*. 4 (2013) 583-592.
20. Matlosz M., Magaino, S., Landolt, D., *Electrochem Soc*. 141 (1994) 410-418.
21. Epelboin I., Keddam, M., *Electrochim Acta*. 17 (1972)177-186.
22. Belkhaouda, M., Bazzi, L., Benlhachemi, A., Salghi, R., Hammouti, B., Kertit, S., *Applied Surface Science* 252 (2006) 7921–7925
23. Dugstad Lunde, L., Videm, K., *CORROSION/94*, 14 (1994) NACE, Houston, TX.
24. Farelas F., Galicia, M., Brown, B., Nestic, S., Castaneda, H., *Corrosion Science*. 52 (2010) 509–517
25. Howard W.P., *Materials Science and Engineering A*. 198 (1995) 213-223.
26. Baptiste J., Orazem, M.E., Pébère, N., Tribollet, B., *Electrochim Acta*. 51(2006) 1473–1479.
27. Al-Hassan S., Mishra, B., Olson, D.L., et al., *NACE International- Corrosion* 54 (1998) 480.
28. Sazou D., Pagitsas, M., *Electrochimica Acta* 38 (1993) 835-845.
29. Kellou-Kerkouche F., Benchettara, A., Amara, S., *Materials Chemistry and Physics*. 110 (2008) 26–33
30. Pagitsas M., Pavlidou, M., Sazou, D., *Electrochimica Acta* 53 (2008) 4784–4795.
31. Song G.-L., Cao, C.-N., Lin, H.-C., *Corros. Sci*. 36 (1994) 1491-1497.
32. Sazou D., Diamantopoulou, D., Pagitsas, M., *Russian Journal of Electrochemistry*. 36 (2000) 1072-1084.
33. Pagitsas M., Sazou, D., *Electroanal. Chem*. 334 (1992) 81-101.
34. Syugaev V., Lomaeva, S.F., Reshetnikov, S.M., *Protection of Metals and Physical Chemistry of Surfaces*. 46 (2010) 82–89.
35. Saltykov S. N., Putilina, M. S., *Protection of Metals*. 42 (2006) 372–377.
36. Lawrence V. O., *New York: Nova Science Publishers*. Ch 3 (2008) 175.
37. Saltykov S. N., Makarov, G. V., Toroptseva, E. L., Filatova, Y. B., *Protection of Metals* 40 (2004) 56–61.
38. Syugaev V., Lomaeva, S. F., Reshetnikov, S. M., Shuravin, A. S., Sharafeeva, E. F., Surnin, D. V., *Protection of Metals*. 44 (2008) 367-371.
39. Liu, W., Zhang, Y., Zhang, H., Qu, Z., Li, J., *Journal of Solid State Electrochemistry*, 13 (2009) 1645-1652.

(2014) ; <http://www.jmaterenvironsci.com/>